ELSEVIER

International Journal of Solids and Structures 41 (2004) 3905–3927

INTERNATIONAL JOURNAL OF SOLIDS and STRUCTURES

www.elsevier.com/locate/ijsolstr

Wave scattering by cracks in inhomogeneous continua using BIEM

G.D. Manolis [a,*], P.S. Dineva [b], T.V. Rangelov [c]

[a] *Department of Civil Engineering, Aristotle University, Panepistimioupolis, P.O. Box 502, Thessaloniki GR-54006, Greece*
[b] *Department of Continuum Mechanics, Institute of Mechanics, Bulgarian Academy of Sciences, 1113 Sofia, Bulgaria*
[c] *Department of Mathematical Physics, Institute of Mathematics and Informatics, Bulgarian Academy of Sciences, 1113 Sofia, Bulgaria*

Received 14 July 2003; received in revised form 16 February 2004
Available online 19 March 2004

Abstract

Elastic wave scattering by cracks in inhomogeneous geological continua with depth-dependent material parameters and under conditions of plane strain is studied in this work. A restricted case of inhomogeneity is considered, where Poisson's ratio is fixed at one-quarter, while both shear modulus and density profile vary with depth, but proportionally to each other. Furthermore, time-harmonic conditions are assumed to hold. For this type of material, the body wave speeds remain macroscopically constant and it becomes possible to recover exact Green functions for the crack-free inhomogeneous continuum by using an algebraic transformation method proposed in earlier work as a first step. In a subsequent step, the complete elastodynamic fundamental solution along with its spatial derivatives and an asymptotic expansion for small argument, are all derived in closed-form using the Radon transform. Next, a non-hypersingular, traction-based boundary integral equation method (BIEM) formulation for solving boundary-value problems with internal cracks is presented. Specifically, the BIEM is used for computing stress intensity factors and scattered wave displacement amplitudes for an inclined line crack in an otherwise inhomogeneous continuum that is being swept by either pressure waves or vertically polarized shear waves at an arbitrary angle of incidence with respect to the horizontal direction. The numerical results obtained herein reveal substantial differences between homogeneous and continuously inhomogeneous materials containing a crack in terms of their dynamic response, where the latter case is assumed to give a more realistic representation of geological deposits compared to the former one. Finally, these types of examples plus the benchmark case used for validation, serve to illustrate the present approach and to show its potential for solving complex problems not just in geophysics, but also in mechanics.

Keywords: Algebraic transformation; Boundary integral equation method; Cracks; Elastic wave scattering; Elastodynamics; Inhomogeneous media; Radon transformation; Stress intensity factor

* Corresponding author. Tel.: +30-2310-995663; fax: +30-2310-995769.
E-mail addresses: gdm@civil.auth.gr (G.D. Manolis), petia@imbm.bas.bg (P.S. Dineva), rangelov@math.bas.bg (T.V. Rangelov).

0020-7683/$ - see front matter © 2004 Elsevier Ltd. All rights reserved.
doi:10.1016/j.ijsolstr.2004.02.030

1. Introduction

Elastic wave propagation through media with complex structure is of paramount importance in various engineering fields, including dynamics of composite materials, non-destructive testing evaluation, geophysical studies of the earth's interior, earthquake-induced ground motion prediction, soil–structure interaction, oil prospecting, etc. (Ewing et al., 1957; Helbig, 1994; Nayfeh, 1995; Panza et al., 2000). Focusing geological continua, the physical problem behind travelling elastic waves involves reflection, refraction, diffraction and scattering phenomena that are difficult to quantify. Additional phenomena that must be accounted for are soil layering (Thomson, 1950; Haskell, 1953; Lysmer and Waas, 1972; Kausel, 1981), material inhomogeneity and anisotropy (Kausel, 1986; Vrettos, 1990, 1991; Fah et al., 1993; Wang and Achenbach, 1993; Kim et al., 1999), material non-linearities (Nowacki, 1978), material periodicity (Sotiropoulos, 1993), and existence of a second phase within the skeleton material (Chen, 1994; Tadeu et al., 2002). The presence of various types of discontinuities (Tadeu et al., 1996) and cracks (Zhang and Gross, 1998) in the soil further increases the complexity of the overall picture. Specifically, cracks not only act as wave refractors and scatterers, but also as stress concentration points. At the crack tips, a square-root stress singularity exists, whose strength is described by the stress intensity factor (SIF) as defined in linear elastic fracture mechanics, and may lead to localized material failure. In general, the complexity of problems involving geological media is such that most of the aforementioned phenomena are examined separately.

During the last few decades, the volume of work on elastic wave propagation in non-homogeneous media has become quite vast, but essentially three groups of methods can be distinguished, namely (i) analytical, (ii) numerical and (iii) hybrid. Analytical methods are based on certain key concepts, such as ray theory (Babich, 1956; Pao and Gajewski, 1977), mode matching techniques (Knopoff, 1964; Schwab and Knopoff, 1970; Panza, 1985) and integral representation theorems (Herrera, 1964). Ray theory and mode matching are effective methods for regions with simple geometry, dimensions larger then the wavelength of the propagating signal, and layered medium structure with slowly varying velocity. An important tool in the numerical analysis of wave motion through irregular 2D soil media is the analytical construction of transmitting boundaries, which is equivalent to a continuation of the finite element mesh used for modeling the medium in question to infinity, with obvious computational advantages (Lysmer and Waas, 1972). An accurate analytical method for obtaining Green's functions (or fundamental solutions) for point forces acting in a layered medium is due to Kausel (1981), which provides a general framework for handling loads of arbitrary spatial–temporal variation by using Fourier and Hankel transforms. This work was later extended (Kausel, 1986) for wave propagation in fully anisotropic, layered media and the resulting functions can be used in numerical simulations of general boundary value problems.

One particularly efficient numerical method that has emerged from integral representation theory is the BIEM (Cruse, 1968), and its use has since been extended to a wide spectrum of dynamic analyses (Beskos, 1997). The advantages of the BIEM are reduction in the dimensions of the problem, implicit satisfaction of the radiation conditions associated with unbounded domains, solution at internal points in the domain exclusively in terms of boundary data, and the possibility to model multi-layered regions with complex geometry with good accuracy (Dominguez, 1993). As such, it is a good candidate for use in problems involving elastic wave propagation through fractured, inhomogeneous geological media (Dineva and Gavrilova, 2000, 2001). Finally, hybrid methods have also been formulated by combining finite elements and boundary elements in an effort to optimize the performance of each constituent method (Bielak et al., 1991; Moczo et al., 1997; Song and Wolf, 1998; Lie et al., 2000).

The mathematical background behind wave motion in non-homogeneous media involves solution of partial differential equations (PDE) with variable coefficients. In general, these equations do not possess explicit and easy to calculate fundamental solutions (or Green's functions), which prevents reduction of the physical boundary-value problem (BVP) to a system of boundary integral equations that can subsequently

be processed by standard numerical quadrature techniques. As far as recent work along these lines is concerned, we mention the work of Vrettos (1990, 1991) on the propagation characteristics of elastic waves (pressure and polarized shear surface waves, Rayleigh waves, etc.) through uniform soil deposits with vertical inhomogeneities of various types, such as bounded exponential shear modulus, a general power law shear modulus, etc. Manolis and Shaw (1996, 2000) derived Green functions for 2D and 3D continua using the relatively simple concept of algebraic transformations. The drawback is that the dynamic solutions recovered are valid for rather restricted cases of inhomogeneity. Also, Mikhailov (2002) constructed a special class of localized matrices (in lieu of a proper fundamental solution), which reduce the general BVP with variable coefficients to a localized integro-differential equation system that is amenable to numerical treatment. Ang et al. (2003) proposed a dual-reciprocity BIEM for numerical solution of 2D problems governed by elliptic-type partial differential equations with variable coefficients, while a multiple crack problem under anti-plane conditions was considered for a class of inhomogeneous anisotropic elastic materials in Ang et al. (1999). Finally, Azis and Clements (2001) derived boundary integral equations for numerical solution of PDE that described the static deformations of inhomogeneous and anisotropic materials.

The basic aim of the present work is development of a non-hypersingular, traction-based BIEM for solving 2D, steady-state elastic wave propagation problems through cracked inhomogeneous geological deposits with material parameters that vary quadratically with respect to the depth coordinate. The ensuing transient elastodynamic analysis is done by synthesizing the frequency domain results. Previous efforts (Dineva and Manolis, 2001) regarding seismic wave propagation in finite-type geological regions with non-parallel layers, surface topography and interface as well as internal cracks, serves as a springboard for this work. That particular problem was solved by a combination of displacement and hypersingular traction BIEM and the numerical results (free-surface displacement field and stress concentration at the crack-tips) were found to be sensitive to various problem parameters and especially to the interaction effect manifested between multiple cracks. The novelty of the present work lies primarily in modeling soil inhomogeneity (Manolis, 2003). Computation of parameters such as crack opening displacement (COD) and stress concentration factor (SIF) yields useful information in understanding the physical processes that develop in geological formations as they are swept by incoming waves and help generalize previously obtained free-field studies and wave diffraction results in the presence of discontinuities.

It should be mentioned at this point that there is recent interest in fracture mechanics problems when the underlying material is no longer homogeneous. For instance, Yue et al. (2003) have studied mode I and II SIF for cracks in functionally graded materials (FGM), whereby two dissimilar homogeneous layers are joined by an intermediate layer with an exponentially varying shear modulus. The static BIEM with a generalized Kelvin solution as its kernel is used, and the influence of both non-homogeneity and layer thickness on the SIFs is studied for elliptical cracks placed at the material interfaces. In Zhang et al. (2003), transient crack analysis in an FGM is studied by using a hypersingular, time domain BIEM. In the absence of an exact Green's function (which may not be available for all types of inhomogeneities), a convolution quadrature formula is adopted for the transient part, while Galerkin's method is applied for the spatial discretization part. Numerical results are recovered for transient SIFs pertaining to a finite crack subjected to impact loading under anti-plane strain conditions. In both works, the influence of inhomogeneity is clearly discerned from the results.

The paper is structured as follows: First, the BVP formulation is given in Section 2. Next, fundamental solutions for the governing equations of motion are obtained in Section 3 by combining an algebraic transformation with the Radon transform. Section 4 presents the non-hypersingular traction BIEM formulation and discusses numerical implementation aspects, including validation studies. A series of numerical examples involving an inclined line crack in an inhomogeneous plane subjected to steady-state pressure (P) and vertically polarized shear (SV) waves with variable incidence angles are then solved in Section 5. Finally, the paper closes with a list of conclusions regarding the aforementioned physical

problem, whose true complexity presents daunting challenges. It should be mentioned in closing that the present method can be applied to other problems in dynamic fracture mechanics, such as non-destructive testing evaluation of man-made materials.

2. Boundary-value problem formulation

Consider an R^2 continuum that is heterogeneous with position-dependent material parameters (e.g., Lamé moduli $\lambda = \lambda(x)$, $\mu = \mu(x)$ and density $\rho = \rho(x)$, where $x = (x_1, x_2)$), as shown in Fig. 1. The governing equations of motion in the absence of body forces and in the frequency domain are

$$\sigma_{ij,j}(x,\omega) + \rho(x)\omega^2 u_i(x,\omega) = 0 \tag{1}$$

where the equilibrium operator is $\sigma_{ij,j}(x,\omega) = \{\lambda(x)u_{k,k}(x,\omega)\}_{,i} + \{\mu(x)(u_{i,j}(x,\omega) + u_{j,i}(x,\omega))\}_{,j}$ (Ewing et al., 1957) and the second term are the inertia forces.

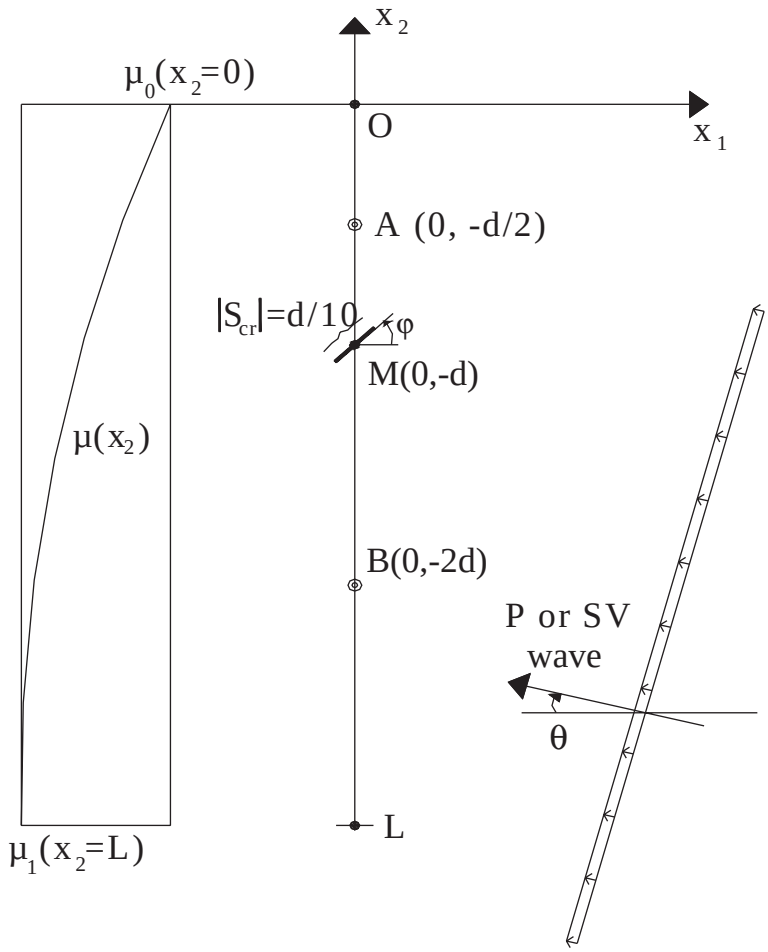

Fig. 1. Incident pressure (*P*) and vertically polarized shear (SV) waves in a cracked inhomogeneous plane.

It is assumed here that (i) the material parameters are functions of only one spatial co-ordinate, namely depth x_2, and more specifically that $\mu(x) = \lambda(x) = h(x)\mu_0$, where $h(x) = (ax_2 + b)^2$; (ii) Poisson's ratio is equal to $\nu = 0.25$; (iii) the material density profile is proportional to the shear modulus profile, i.e., $\rho(x)/\mu(x) = \rho_0/\mu_0$ or more precisely, $\rho(x) = \rho_0 h(x)$, where μ_0, $\rho_0 > 0$ and a, b are constants. The null subscript indicates reference values that must be prescribed, while the homogeneous case corresponds to the value $a = 0$. The equations of motion (1) form an elliptic system of PDE, except along line $x_2 = -b/a$, where they degenerate.

Let $S_{\rm cr} \subset R^2$ define a crack as an open arc, i.e., $S_{\rm cr} = S_{\rm cr}^+ \cup S_{\rm cr}^-$. The angle of the crack with respect to the horizontal axis Ox_1 is $\varphi \in (-\pi/2, \pi/2)$, while the incident elastic waves trace an angle θ from Ox_1 (see Fig. 1). It is assumed that the crack does not intersect the line $x_2 = -b/a$, i.e.,

$$S_{\rm cr} \cap \{x_2 = -b/a\} = \emptyset \tag{2}$$

Also, the crack is traction-free

$$t_i|_{S_{\rm cr}} = 0 \tag{3}$$

where tractions $t_i = \sigma_{ij} n_j$ and n_j is the unit normal vector on $S_{\rm cr}^+$. The stress tensor is equal to $\sigma_{ij} = C_{ijkm} u_{k,m}$, with $C_{ijkm} = h(x) C^0_{ijkm}$, and $C^0_{ijkm} = \mu_0(\delta_{ij}\delta_{km} + \delta_{ik}\delta_{jm} + \delta_{im}\delta_{jk})$ the standard form for a homogeneous continuum.

In earlier work, Manolis and Shaw (1996) derived an algebraic transformation for the displacement vector of the type

$$u_i(x,\omega) = h^{-1/2}(x) U(x,\omega) \quad \text{in } R^2 \setminus \{x_2 = -b/a\} \tag{4}$$

where $U(x,\omega)$ is a solution for the dynamic equilibrium equations expressed in terms of the equivalent homogeneous medium case as

$$\Sigma_{ij,j} + \rho(x)\omega^2 U_i = 0 \tag{5}$$

The corresponding equilibrium operator here is $\Sigma_{ij,j} = \mu(x) U_{i,jj} + 2\mu(x) U_{j,ij}$. Also, the traction-free boundary condition of Eq. (3) written for $U(x,\omega)$ is as follows:

$$h(x) C^0_{ijkm} n_j \left(\mu^{-1/2}(x) U_k\right)_{,l}\Big|_{S_{\rm cr}} = 0 \tag{6}$$

We note that the above boundary condition does not degenerate due to the presence of Eq. (2), i.e., $\mu(x)|_{S_{\rm cr}} \neq 0$. This is known as a boundary condition of the third type (Ladyzenskaja and Urall'tzeva, 1973). Next, proceeding as in Wendland and Stephan (1990), it can be shown that the BVP defined by Eqs. (5) and (6) has a weak solution in an appropriate Sobolev space and that this solution is unique if a Sommerfeld-type radiation condition is satisfied at infinity (Vainberg, 1982).

Our aim here is to find a solution of the BVP defined by Eqs. (1) and (3) by utilizing the BIEM, which in turn is formulated in terms of the ancillary (transformed) problem defined by Eqs. (5) and (6). This BIEM solution will yield the jump in the displacement field across the crack (i.e., the COD) and the SIF at the crack tip for an inclined crack buried in the inhomogeneous plane as it is swept by incoming elastic waves.

3. Fundamental solutions for the inhomogeneous continuum

We will first derive fundamental solutions for the displacements and tractions and then compute their asymptotic form for small argument.

3.1. Displacement and traction fundamental solutions

A fundamental solution (or Green's function) $U^*_{ij}(x,\xi)$ for Eq. (5) is a solution of the following transformed PDE system:

$$\Sigma^*_{ijk,j} + \rho_0\omega^2 U^*_{ik} = -h^{-1/2}(\xi)\delta(x-\xi) \tag{7}$$

which is defined in domain $\left(R^2_x \setminus \{x_2 = -b/a\}\right) \times \left(R^2_\xi \setminus \{\xi_2 = -b/a\}\right)$. Similarly, fundamental solution $u^*_{ij}(x,\xi) = h^{-1/2}(x)U^*_{ij}$ is the original Green's function corresponding to the PDE system defined in the physical domain, i.e.,

$$\sigma^{*x}_{ijk,j} + \rho(x)\omega^2 u^*_{ik} = -\delta(x-\xi) \tag{8}$$

in domain $\left(R^2_x \setminus \{x_2 = -b/a\}\right) \times \left(R^2_\xi \setminus \{\xi_2 = -b/a\}\right)$. In terms of notation, superscript x in $\sigma^{*x}_{ijk,j}$ indicates differentiation with respect to spatial coordinate x, while $\delta(x,\xi) = \delta(x_1-\xi_1)\delta(x_2-\xi_2)$ is the Dirac delta function in 2D.

Eq. (7) is solved by the Radon transform (Zayed, 1996), which is defined in the space of rapidly decreasing functions as

$$\hat{f}(s,m) = R(f) = \int_{\langle x,m\rangle = s} f(x)\,\mathrm{d}x = \int f(x)\delta(s - \langle x,m\rangle)\,\mathrm{d}x \tag{9}$$

and where $\langle,\rangle$ denotes the scalar product in R^2.

The inverse Radon transform is $R^{-1}\left(\hat{f}\right) = R^*\left(K\hat{f}\right)$ where

$$\tilde{f}(s,m) = K\hat{f} = \int_{-\infty}^{\infty} \frac{\partial_\sigma f(\sigma,m)}{s-\sigma}\,\mathrm{d}\sigma \tag{10}$$

and

$$R^*\left(\tilde{f}\right) = \frac{1}{4\pi^2}\int_{|m|=1} \tilde{f}(s,m)|_{s=\langle x,m\rangle}\,\mathrm{d}m \tag{11}$$

The Radon transform is linear, i.e., $R(\alpha f + \beta g) = \alpha R(f) + \beta R(g)$, differentiation is defined as $R(\partial_{x_j} f) = m_j \partial_s \hat{f}(s,m)$, and finally Dirac's delta function transforms as $R(\delta(x)) = \delta(s)$. We mention at this point that the Radon transform was recently used by the authors (Manolis et al., 2003) in the derivation of fundamental solutions for the non-homogeneous biharmonic equation governing bending of plates supported on an elastic half-space.

The PDE system given by Eq. (7) can be written in compact form using matrix notation as follows:

$$(L(\partial) + \rho_0\omega^2)U^* = -\frac{1}{h^{1/2}(x)}\delta(x,\xi) \tag{12}$$

where

$$L(\partial) = \mu_0 \begin{pmatrix} 3\partial^2_{11} + \partial^2_{22} & 2\partial^2_{12} \\ 2\partial^2_{21} & \partial^2_{11} + 3\partial^2_{22} \end{pmatrix}$$

Given that the source (or load point) is $\xi \in R^2_\xi \setminus \{\xi_2 = -b/a\}$ and the receiver (or field point) is $x \in R^2_x \setminus \{x_2 = -b/a\}$, the above right-hand side becomes

$$-\frac{1}{h^{1/2}(x)}\delta(x,\xi) = \begin{cases} 0, & x \neq \xi \\ -\frac{1}{h^{1/2}(\xi)}\delta(0), & x = \xi \end{cases}$$

which implies that:

$$\frac{1}{h^{1/2}(x)}\delta(x,\xi)=\frac{1}{h^{1/2}(\xi)}\delta(x,\xi) \tag{13}$$

The next step is to define

$$\widehat{U}=R(U^*),\quad L(m)=\mu_0\begin{pmatrix}3m_1^2+m_2^2 & 2m_1m_2\\ 2m_1m_2 & m_1^2+3m_2^2\end{pmatrix}$$

with $|m|=1$. Since $R(\delta(x,\xi))=\int\delta(x,\xi)\delta(s-\langle x,m\rangle)\,\mathrm{d}x=\delta(s-\langle m,\xi\rangle)$, application of the Radon transform to both sides of Eq. (12) yields

$$\left(L(m)\partial_s^2+\rho_0\omega^2\right)\widehat{U}=-\frac{1}{h^{1/2}(\xi)}\delta(s-\langle m,\xi\rangle)I_2 \tag{14}$$

where I_2 is the unit matrix in 2D.

In order to solve Eq. (14), it is necessary to transform $L(m)$ into canonical form. To that purpose, the eigenvalues of operator $L(m)$ are computed as $a_1=3\mu_0$, $a_2=\mu_0$, and the corresponding normalized eigenvectors are $\gamma_1=(m_1,m_2)$, $\gamma_2=(-m_2,m_1)$, obeying the usual conditions of $\gamma_1\perp\gamma_2$, $|\gamma_j|=1$. The eigenvector matrix is denoted as

$$T=\begin{pmatrix}m_1 & -m_2\\ m_2 & m_1\end{pmatrix}$$

which implies that the inverse is equal to the transpose, i.e.,

$$T^{-1}=T^{\mathrm{t}}=\begin{pmatrix}m_1 & m_2\\ -m_2 & m_1\end{pmatrix}$$

and that $T\widehat{U}=\widehat{V}$, where $\widehat{V}$ is the fundamental solution corresponding to the uncoupled equations of motion. Left-hand side multiplication of Eq. (14) by T^{-1} gives

$$\left(A\partial_s^2+\rho_0\omega^2 I_2\right)\widehat{V}=-\frac{1}{h^{1/2}(\xi)}T^{-1}\delta(s-\langle m,\xi\rangle) \tag{15}$$

where

$$A=T^{-1}L(m)T=\begin{pmatrix}a_1 & 0\\ 0 & a_2\end{pmatrix}=\begin{pmatrix}3 & 0\\ 0 & 1\end{pmatrix}$$

is the diagonal operator indicating uncoupling of the transformed equations of motion. Eq. (15) are essentially four ordinary differential equations of the type

$$\left(a_0\partial_s^2+b_0\right)\hat{w}=\gamma_0\delta(s-\tau) \tag{16}$$

Following Vladimirov (1984), the solution of Eq. (16) can be obtained in the following form:

$$\hat{w}=\alpha_0\gamma_0\mathrm{e}^{\mathrm{i}k|s-\tau|},\quad \alpha_0=\frac{\mathrm{i}}{2a_0k},\quad k=\sqrt{\frac{b_0}{a_0}}. \tag{17}$$

The next step is to apply the inverse Radon transform to Eq. (17) and recover

$$\tilde{w}=K(\hat{w})=\alpha_0\gamma_0\left[\mathrm{i}\pi\mathrm{e}^{\mathrm{i}z}-2(\mathrm{ci}(z)\cos(z)+\mathrm{si}(z)\sin(z)\right],\quad z=|k(s-\tau)| \tag{18}$$

where $\mathrm{ci}(z)=-\int_z^\infty\frac{\cos t}{t}\,\mathrm{d}t$, $\mathrm{si}(z)=-\int_z^\infty\frac{\sin t}{t}\,\mathrm{d}t$ respectively are the cosine and sine integral functions. The last step involves using Eq. (11) in conjunction with Eq. (18) for recovering fundamental solution $U_{ij}^*(x,\xi)$ and its derivatives $U_{ij,k}^*(x,\xi)$ in the domain defined by the algebraic transformation. Specifically, we obtain

$$U^*(x,\xi)=\frac{1}{4\pi^2}\int_{|m|=1}\begin{pmatrix} m_1 & m_2\\ -m_2 & m_1\end{pmatrix}\begin{pmatrix} m_1\tilde{u}_1 & -m_2\tilde{u}_1\\ m_2\tilde{u}_2 & m_1\tilde{u}_2\end{pmatrix}\Bigg|_{s=|\langle m,x-\xi\rangle|}\mathrm{d}m, \tag{19}$$

and

$$U^*_{,k}(x,\xi)=\frac{1}{4\pi^2}\int_{|m|=1}\begin{pmatrix} m_1 & m_2\\ -m_2 & m_1\end{pmatrix}\begin{pmatrix} m_1\partial_s\tilde{u}_1 & -m_2\partial_s\tilde{u}_1\\ m_2\partial_s\tilde{u}_2 & m_1\partial_s\tilde{u}_2\end{pmatrix}\Bigg|_{s=|\langle m,x-\xi\rangle|} m_k\,\mathrm{sgn}(\langle m,x-\xi\rangle)\,\mathrm{d}m \tag{20}$$

with $k=1,2$. In the above, the intermediate functions are

$$\tilde{u}_j(s,m,\xi)=\frac{1}{h^{1/2}(\xi)}\frac{1}{2a_j}\left\{\mathrm{i}\pi\mathrm{e}^{\mathrm{i}k_js}-2\left[\mathrm{ci}(k_js)\cos(k_js)+\mathrm{si}(k_js)\sin(k_js)\right]\right\}=\frac{1}{h^{1/2}(\xi)}u^1_j(s,m)$$

$$\partial_s\tilde{u}_j(s,m,\xi)=\frac{1}{h^{1/2}(\xi)}\frac{1}{2a_j}\left\{-\pi k_j\mathrm{e}^{\mathrm{i}j s}-\frac{2}{s}+2k_j\left[\mathrm{ci}(k_js)\sin(k_js)-\mathrm{si}(k_js)\cos(k_js)\right]\right\}=\frac{1}{h^{1/2}(\xi)}\partial_s u^1_j(s,m)$$

and $u^1_j(s,m)=(1/2a_j)\{\mathrm{i}\pi\mathrm{e}^{\mathrm{i}k_js}-2[\mathrm{ci}(k_js)\cos(k_js)+\mathrm{si}(k_js)\sin(k_js)]\}$ with $k_j=\sqrt{\rho_0/a_j}\omega$.

What is now left is the simple, inverse algebraic transformation for returning to the original physical domain. Thus, by combining Eqs. (4), (19) and (20), we obtain the fundamental solution of Eq. (8) and its derivatives as

$$u^*_{ij}(x,\xi)=h^{-1/2}(x)h^{-1/2}(\xi)U^*_{ij}(x,\xi) \tag{21}$$

and

$$\sigma^{*z}_{ijk}(x,\xi)=h(z)C^0_{ijml}u^{*z}_{mk,l}(x,\imath),\quad z=x\text{ or }\xi \tag{22}$$

where $u^{*x}_{mk,l}(x,\xi)=(h^{-1/2}(x))_{,l}h^{-1/2}(\xi)U^*_{mk}+h^{-1/2}(x)h^{-1/2}(\xi)U^{*x}_{mk,l}$ and finally $u^{*\xi}_{mk,l}(x,\xi)=(h^{-1/2}(\xi))_{,l}$-$h^{-1/2}(x)U^*_{mk}+h^{-1/2}(x)h^{-1/2}(\xi)U^{*\xi}_{mk,l}$.

It is observed that the fundamental solution and its derivatives for the inhomogeneous case in Eqs. (21) and (22) depend not only on the difference $x-\xi$ as in the homogeneous case, but also on x and ξ separately. We finally note that symmetry in the form $U^{*x}_{mk,l}=U^{*\xi}_{mk,l}$ holds, and mention in passing that a fundamental solution for the anisotropic, yet otherwise homogeneous continuum was obtained using the Radon transform by Wang and Achenbach (1994).

3.2. Asymptotic behavior of the fundamental solution

At this point, we also need the asymptotic expansions for the fundamental solution and its derivatives. When field point $x\to\xi$, continuity in h implies that $h(x)=h(\xi)+\mathrm{O}(|x-\xi|)$. Thus, from Eqs. (21) and (22) it is possible to obtained the reduced forms

$$u^{*\mathrm{as}}_{ij}=h^{-1}(\xi)U^{*\mathrm{as}}_{ij}=h^{-1}(\xi)b_{ij}\ln|x-\xi|, \tag{23}$$

$$\sigma^{*\mathrm{as}}_{ijm}=C_{ijkl}u^{*\mathrm{as}}_{mk,l} \tag{24}$$

where $u^{*\mathrm{as}}_{mk,l}=\left(h^{-1/2}(\xi)\right)_{,l}h^{-1/2}(\xi)b_{mk}\ln|x-\xi|+h^{-1}(\xi)\eta_{mkl}1/|x-\xi|$. Then,

$$\begin{aligned}\sigma^{*\mathrm{as}}_{ijm}&=C_{ijkl}(\xi)\left[h^{-1/2}(\xi)(h^{-1/2}(\xi))_{,l}b_{mk}\ln|x-\xi|+h^{-1}(\xi)\eta_{mkl}\frac{1}{|x-\xi|}\right]\\&=C^0_{ijkl}\left[-\frac{1}{2}h^{-1}(\xi)(h(\xi))_{,l}b_{mk}\ln|x-\xi|+\eta_{mkl}\frac{1}{|x-\xi|}\right]\end{aligned} \tag{25}$$

4. Numerical solution of the BVP

Solution of BVP for dynamic fracture of a finite, inclined line crack in an inhomogeneous continuum swept by elastic waves is accomplished by numerical implementation of a BIEM formulation in 2D.

4.1. Non-hypersingular traction BIEM

The BVP defined by Eqs. (1)–(3) will now be recast into a system of integro-differential equations for computing crack parameters such as the COD and, as a second step, the SIF. Specifically, let u_i be the total displacement field solution of Eqs. (1)–(3) given as $u_i = u_i^{\text{in}} + u_i^{\text{sc}}$, where u_i^{in} is the incident wave field, which in turn is a particular solution of Eq. (1). Furthermore, u_i^{sc} is the elastic wave field that is scattered by the crack. Following Zhang and Gross (1998), we derive a set of displacement and traction boundary integral equations (BIE) by using the equivalent divergence form of Eq. (1) and by assuming that both displacements and tractions u_i, t_i satisfy Sommerfeld's radiation condition at infinity. The integral form for the scattered field is

$$u_i^{\text{sc}}(x) = -\int_{S_{\text{cr}}} \sigma_{kji}^{*y}(y,x)\,\Delta u_k(y) n_j(y)\,\mathrm{d}S_y \tag{26}$$

for a given field point $x \notin S_{\text{cr}}^+$ and $x \in R^2 \setminus \{x_2 = -b/a\}$. The stress tensor is given as $\sigma_{kji}^{*z}(y,x) = C_{kjml}(z) u_{mi,l}^{*z}(y,x)$, where strains are defined by $u_{mi,l}^{*z} = \frac{\partial}{\partial z_l} u_{mi}^{*}$ and $z = y$ or x. Also, the corresponding scattered traction field is

$$t_{\text{p}}^{\text{sc}}(x) = -C_{pqil}(x) n_q(x) \int_{S_{\text{cr}}} \sigma_{kji,l}^{*y}(y,x)\,\Delta u_k(y) n_j(y)\,\mathrm{d}S_y. \tag{27}$$

In view of the boundary condition $t_{\text{p}}^{\text{sc}} = -t_{\text{p}}^{\text{in}}$ given by Eq. (3), and using similar arguments as Zhang and Gross (1998) regarding conservation law integrals, we obtain the following non-hypersingular traction BIE formulation for field point $x \in S_{\text{cr}}^+$:

$$t_i^{\text{in}}(x) = C_{ijkl}(x) n_j(x) \int_{S_{\text{cr}}} \left(\left[\sigma_{p\eta k}^{*y}(y,x)\,\Delta u_{p,\eta}(y) - \rho(y)\omega^2 u_{dk}^{*}(y,x)\,\Delta u_d(y) \right] \delta_{\lambda l} n_\lambda(y) - \sigma_{m\lambda k}^{*y}(y,x)\,\Delta u_{m,l}(y) n_\lambda(y) \right) \mathrm{d}S_y \tag{28}$$

The primary unknowns in the above equation are the crack interface displacements and strains Δu_k, $\Delta u_{k,l}$. We note that in contrast to the homogeneous case, the fundamental solution and its derivatives computed here depend on the relative distance between source and receiver $(x - y)$, as well as on the field point positions x and y separately.

4.2. Numerical implementation

The above non-hypersingular, traction-based BIE given in Eq. (28) will now be used to represent the complete BVP, which consists of an unbounded inhomogeneous geological deposit containing an inclined crack. All surface discretization schemes are accomplished by using just two types of line boundary elements (BE), namely: (i) the standard parabolic element for all surfaces excluding crack-tips; (ii) the quarter-point element to model the asymptotic behavior of the displacement field in the vicinity of the crack tip. These two BE, along with the Green's functions derived in Section 3, are the basic building blocks for generating an efficient BIEM software code to recover the steady-state, scattered elastic wave fields around the buried cracks. Although the formulation is for time-harmonic conditions, it is always possible to capture the transient nature the phenomenon by standard Fourier synthesis (Manolis and Beskos, 1987).

At first, the scattered displacement field at any point in the unbounded domain is obtained following a BVP solution of Eq. (28) for the COD, which is subsequently substituted in Eq. (26) for recovering u_i^{sc}. Next, the dynamic SIFs are also calculated in a second step, following solution for the COD and using the traction vector t_i from the BVP at a given small distance r ahead of the crack tip (Aliabadi and Rooke, 1991) as $K_I = \lim_{r\to 0} t_2(x)\sqrt{2\pi r}$ and $K_{II} = \lim_{r\to 0} t_1(x)\sqrt{2\pi r}$ for Modes I and II, respectively. The SIF is then normalized by its static value. More details on the above numerical implementation can be found elsewhere (Rangelov et al., 2003).

Next, the accuracy and convergence characteristics of the proposed BIEM are established in the next section by gauging the solution obtained for the benchmark problem of a buried, inclined line crack in an elastic homogeneous half-plane subjected to incident time-harmonic P and SV waves. Following that, a series of parametric studies are conducted for the inclined crack in an inhomogeneous medium in order to quantify the sensitivity of the scattered wave field as well as of the stress concentration effect around the buried crack to various problem-specific parameters, such as degree of soil inhomogeneity, crack inclination angle with respect to the horizontal and dynamic characteristics of the incident elastic waves.

5. Numerical examples

The non-hypersingular, traction-based BIEM presented in the previous section will now be used to examine crack-wave interaction phenomena in a 2D inhomogeneous plane due to incoming P and SV waves under time-harmonic conditions.

5.1. Material profiles

The various constraints that appeared during the fundamental solution procedure outlined in Sections 2 and 3 will now be examined in detail. It was established that the elastic parameter profiles are quadratic functions of the depth coordinate x_2, given in terms of function $h(x)$, and that $\nu = 0.25$. Constants a, b appearing in $h(x)$ are determined from values at two reference points corresponding to a source–receiver pair located at depths $x_2 = 0$ and $x_2 = L$, respectively, as shown in Fig. 1. Therefore, given that $\mu(0,0) = \mu_0$ and $\mu(0,L) = \mu_1$, we obtain the following profiles:

$$\lambda(x) = \mu(x) = \left(\left(\sqrt{\mu_1} - \sqrt{\mu_0}\right)(x_2/L) + \sqrt{\mu_0}\right)^2 \tag{29}$$

Since the density profile is proportional to that of the elastic parameters, the two body wave speeds, $C_P(x) = \sqrt{3\mu_0/\rho_0}$ and $C_S(x) = \sqrt{\mu_0/\rho_0}$, are macroscopically constant.

In the present example, we consider an unbounded, firm soil deposit with background material properties of $\mu_0 = \lambda_0 = 180 \times 10^6$ N/m^2 and $\rho_0 = 2000$ kg/m^3, giving $C_P = 520$ m/sec and $C_S = 300$ m/sec. Two basic shear modulus profiles are examined here, namely one where the material becomes stiffer and one where it becomes softer with increasing depth. More specifically, $\mu(0,L) = 1.5\mu_0 = 270 \times 10^6$ Pa in the former case (corresponding to a 50% increase) and $\mu(0,L) = 0.75\mu_0 = 135 \times 10^6$ Pa in the latter case (corresponding to a 25% decrease), where the depth scale is chosen as either $L = L_1 = 520$ m or $L = L_2 = 40$ m. The first length scale (L_1) over which the profiles vary coincides with the wavelength of the P wave for the background material at an excitation frequency of 1.0 Hz, while the second length scale (L_2) is much shorter and corresponds to higher frequencies of vibration. Thus, with regards to function $h(x) = (ax_2 + b)^2$, $b = -1$ and a is determined from values of the shear modulus at distance L from the reference point. For instance, this gives $a = \left(\sqrt{1.5} - 1\right)/L$ for the stiffer profile and $a = \left(\sqrt{0.75} - 1\right)/L$ for the softer one. Finally, consider an embedded line crack of length $|S_{cr}| = 10$ m, centered at point M $(0, d = -100)$ and forming an angle $\varphi \in (-\pi/2, \pi/2)$ with respect to the horizontal axis Ox_1 (see Fig. 1).

5.2. Incident wave field

For an incident planar P or SV wave, propagating at a direction angle θ with respect to the horizontal, a solution of the system of Eq. (1) yields

$$u_j^{\text{in}}(x,\omega) = h^{-1/2}(x) U_j^{\text{in}}(x,\omega) \tag{30}$$

where displacement

$$U^{\text{in}}(x,\omega) = D(-\text{i}k_{\text{P}}) \left\{ \begin{array}{c} \cos\theta \\ \sin\theta \end{array} \right\} \text{e}^{-\text{i}k_{\text{P}}(x_1\cos\theta + x_2\sin\theta)}$$

for the P wave and

$$U^{\text{in}}(x,\omega) = D(-\text{i}k_s) \left\{ \begin{array}{c} \sin\theta \\ -\cos\theta \end{array} \right\} \text{e}^{-\text{i}k_s(x_1\cos\theta + x_2\sin\theta)}$$

for the SV wave. In the above, the two wave numbers are $k_{\text{P}} = \omega/C_{\text{P}}$, $k_{\text{S}} = \omega/C_{\text{S}}$ (previously referred to as k_1, k_2) and D is the amplitude of motion. The corresponding incident tractions t_i^{in} are

$$\begin{aligned} t_i^{\text{in}}(x,\omega) &= C_{ijkl}(x) n_j(x) \left(h^{-1/2}(x) U_k^{\text{in}}(x,\omega)\right)_{,l} \\ &= h(x) C_{ijkl}^0 n_j(x) \left[-\frac{1}{2} h^{-3/2}(x) h_{,l}(x) U_k^{\text{in}}(x,\omega) + h^{-1/2}(x) U_{k,l}^{\text{in}}(x,\omega) \right] \end{aligned} \tag{31}$$

Note that the incident P wave solution of Eq. (30), and the resulting tractions given in Eq. (31), are both influenced by material inhomogenity through the presence of function $h(x)$ and its derivatives. Strictly speaking, there is no true plane wave solution in the inhomogeneous case. Thus, we use an incident function of the type given by Eq. (30), which is the simplest possible solution of governing equation (1), in order to recover the boundary conditions of Eq. (3) and then use the traction BIE formulation (see Eq. (28)) for the numerical examples.

5.3. Numerical modeling details

At first, the SIF for a nonhomogeneous material described by function $h(x)$ is calculated using a traction formula (as mentioned in Section 4.2) and subsequently normalized by the following factor:

$$N = \omega^2 N_2 + \omega N_1 \tag{32}$$

In the above,

$$N_1 = \frac{1}{2} h^{-1/2}(x_q) |h_{,2}(x_q)| (\lambda_0 + 2\mu_0) \frac{1}{C_{\text{p}}}, \quad N_2 = h^{1/2}(x_q) \mu_0 \frac{1}{C_s^2}$$

and x_q is the point just ahead of the crack-tip where tractions are calculated. We note that the leading term in N is $\omega^2 N_2$ for $\omega \gg \frac{1}{2} h^{-1}(x_q) |h_{,2}(x_q)| C_{\text{p}}$, while it becomes equal to ωN_1 for $\omega \ll \frac{1}{2} h^{-1}(x_q) |h_{,2}(x_q)| C_s$. Moreover, the behavior of the dynamic solution for $\omega \to 0$ is of the order $\text{O}(\omega)$, in contrast with the homogeneous case, where it behaves as $\text{O}(\omega^2)$. The influence of inhomogenity when $|h_{,2}(x_q)| \neq 0$ on the dynamic solution for $\omega \to 0$ dictates a normalization of the solution by the factor given in Eq. (32). This formula also gives a maximum value for the stress acting on the incident plane wave front, which is assumed to remain finite as $\omega \to 0$. Finally, the amplitude of the scattered displacement field is computed directly using Eq. (26), after inserting the COD recovered from the solution of Eq. (28).

The details of the numerical scheme used in this work have been described by Rangelov et al. (2003), so here we give some basic information pertinent to the present BVP. In particular, five BE are used for

modeling the crack in the following way: The first BE is a left quarter-point element, i.e., an LQP-BE; the second through fourth are ordinary BE; finally, the fifth is a right quarter-point element, i.e.; an RQP-BE. The lengths of these five boundary elements are $l_1 = 0.75,\ l_2 = 2.8,\ l_3 = 2.9,\ l_4 = 2.8,\ l_5 = 0.75$ (m), respectively. Also, the ξ-co-ordinates of the shifted nodal points are $\xi = 0.95$ on the first and second BE and $\xi = -0.95$ on the fourth and fifth BE, while for an ordinary quadratic BE the nodal points are at the two edges and at the center. Finally, we mention that the fundamental solutions were evaluated using the symbolic manipulation software Mathematica (1996), while the BIEM implementation software was produced by using standard Fortran programming (Lahey Fortran 95, 2000).

5.4. Numerical examples

The parametric study presented here investigates the sensitivity of the far-field scattered waves and of the SIF in three different continua with a crack, namely the homogeneous, the stiffening (with increasing depth) and the softening one. The key parameters identified for the study are (i) orientation angle $\varphi \in (-\pi/2, \pi/2)$ of the crack with respect to the horizontal Ox_1 axis; (ii) incoming wave incidence angle θ with respect to Ox_1; and (iii) the material properties as given by dimensionless function $h(x)$ ($=1$ for the homogeneous case), which is set up for two different values of depth scale L. Note that normalization of the dynamic SIF is done by using its static value for the homogeneous material, i.e., $a = 0$, $b = -1$.

At first, Fig. 2 is a validation study that shows SIF (both modes I and II) for the homogeneous continuum normalized with respect to their corresponding static values, versus dimensionless frequency $k_P\alpha$ (where $\alpha = 0.5|S_{cr}| = 5$ m is the half-length of the crack), for different values of the incident wave angle θ and for a horizontal line crack ($\phi = 0$). This particular example serves to gauge the proposed non-hypersingular traction BIEM with the new frequency-dependent, elastodynamic fundamental solution derived in a closed-form by algebraic and Radon transforms. The results are compared with the analytical solution of Chen and Sih (1977). We observe in all the plots of Fig. 2, i.e., (a)–(d), an excellent agreement between the two groups of results, which are obtained by what are essentially two very different methods, across the entire frequency range of interest. In most instances the agreement is to within plotting accuracy, although in a few isolated cases (usually at high $k_P\alpha$ values) there is some divergence of the order of 1–3%.

Next, Figs. 3 and 4 give a normalized SIF (again both modes I and II) for the inhomogeneous continuum versus dimensionless frequency, and more specifically at the left crack-tip of a finite crack, inclined by $\varphi = 45°$ with respect to the horizontal, and for wave incidence angles of $\theta = \pi/2$ and $\theta = \pi/3$, respectively. More specifically, curves 1 through 5 in each plot are for the following sub-cases: Curve 1 is for the 'background' homogeneous case; curves 2 and 4 are for the stiffening material at two different depth scales of $L_1 = 520$ m and $L_2 = 40$ m; and curves 3 and 5 are for the softening material with $L_1 = 520$ m and with $L_2 = 40$ m, respectively. Finally, the (a) and (b) sets of plots (for Mode I and II cracks) are derived for an incident P-wave, while the (c) and (d) sets of plots (again for Modes I and II) are for the SV-wave. The effect of inhomogeneity is now clearly seen: Curves 1 through 3 are closely grouped together, and are bracketed from above and below by curves 4 and 5. Since curve 4 is for the stiffening material across a short depth scale ($L_2 = 40$ m), it is reasonable to expect that it will yield the smallest SIF value. At the other end, we have curve 5 for the softening material with depth scale $L_2 = 40$ m, which yields maximum SIF values. In sum, all plots are consistent with the fact that the SIF changes significantly (with respect to values recorded for the homogeneous 'background' material) when the effect of inhomogeneity is most pronounced, (i.e., when material properties vary rapidly over short distances), and less so when we have a 'milder' shear modulus profile (i.e., a longer depth scale of $L_1 = 520$ m). Table 1 gives a good picture of this situation at three selected values of $k_P\alpha$ (0.1, 0.5 and 1.0), where it is observed that, on the average, the overshoot in all SIFs (save for the SV-wave Mode II SIF) when referred to homogeneous background values, is about +67% and −33% for the rapidly softening and stiffening profiles, respectively. This last SIF shows a far

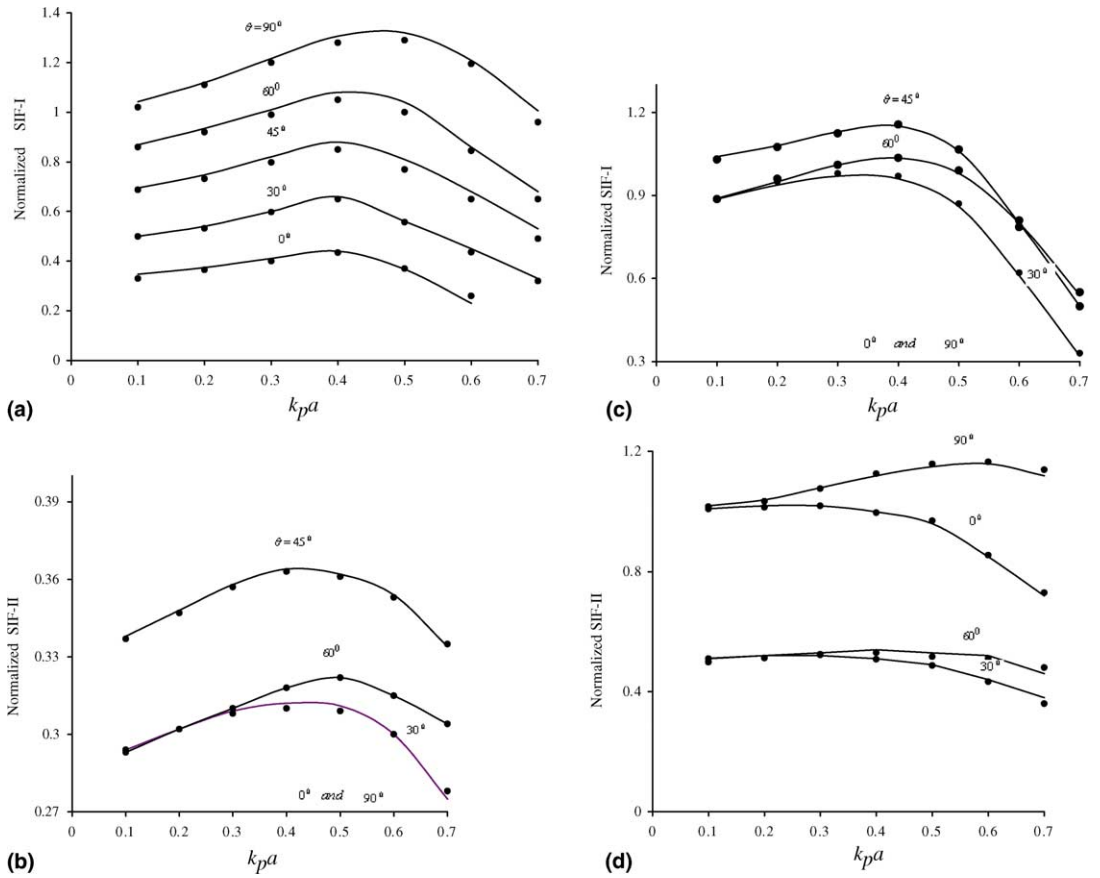

Fig. 2. SIF versus frequency at the left crack-tip of a line crack tracing angle $\varphi = 0$ with respect to the Ox_1-axis: Curves 1 through 5 correspond to incident wave angles $\theta = 0$; $\pi/2$; $\pi/3$; $\pi/6$; $\pi/4$ for (a,b) an incident P-wave and (c,d) an incident SV-wave. Also, (– ● –) the Chen and Sih (1977) results.

more pronounced overshoot of +1000% and −250%, respectively. Compared to all these values, the milder profile yields minor differences when compared to the homogeneous case.

In Fig. 5, we show the normalized SIF for the inhomogeneous continuum versus incident wave angle, at the left crack-tip of a finite crack inclined by $\varphi = 45°$, and at a fixed dimensionless frequency $k_P\alpha = 5.0$ that corresponds to a rather high frequency of vibration of 82.7 Hz. As before, curves 1 through 5 plot the following sub-cases: Curve 1 is for homogeneous material, while the pairs 2 and 4 and 3 and 5 are for stiffening and softening material, respectively, where the shear modulus varies across depth scales of 520 m and 40 m in each pair. Also, the (a) and (b) sets of plots are for the incident P-wave and the (c) and (d) sets are for the SV-wave, each set depicting the two crack modes previously mentioned. The effect of material inhomogeneity observed here is consistent with that seen in all previous figures. Specifically, maximum and minimum SIF values are respectively obtained for both softening and stiffening materials across the short depth scale of $L = 40$ m. The homogeneous material SIF is bracketed by those results, while the effect of inhomogeneity is less pronounced across the larger depth scale of $L = 520$ m. As before, Table 2 summarizes the maximum overshoot observed in the SIFs, in reference to the homogeneous background, for the full range of incident wave angles at that particular frequency. We see an average overshot of about 50%

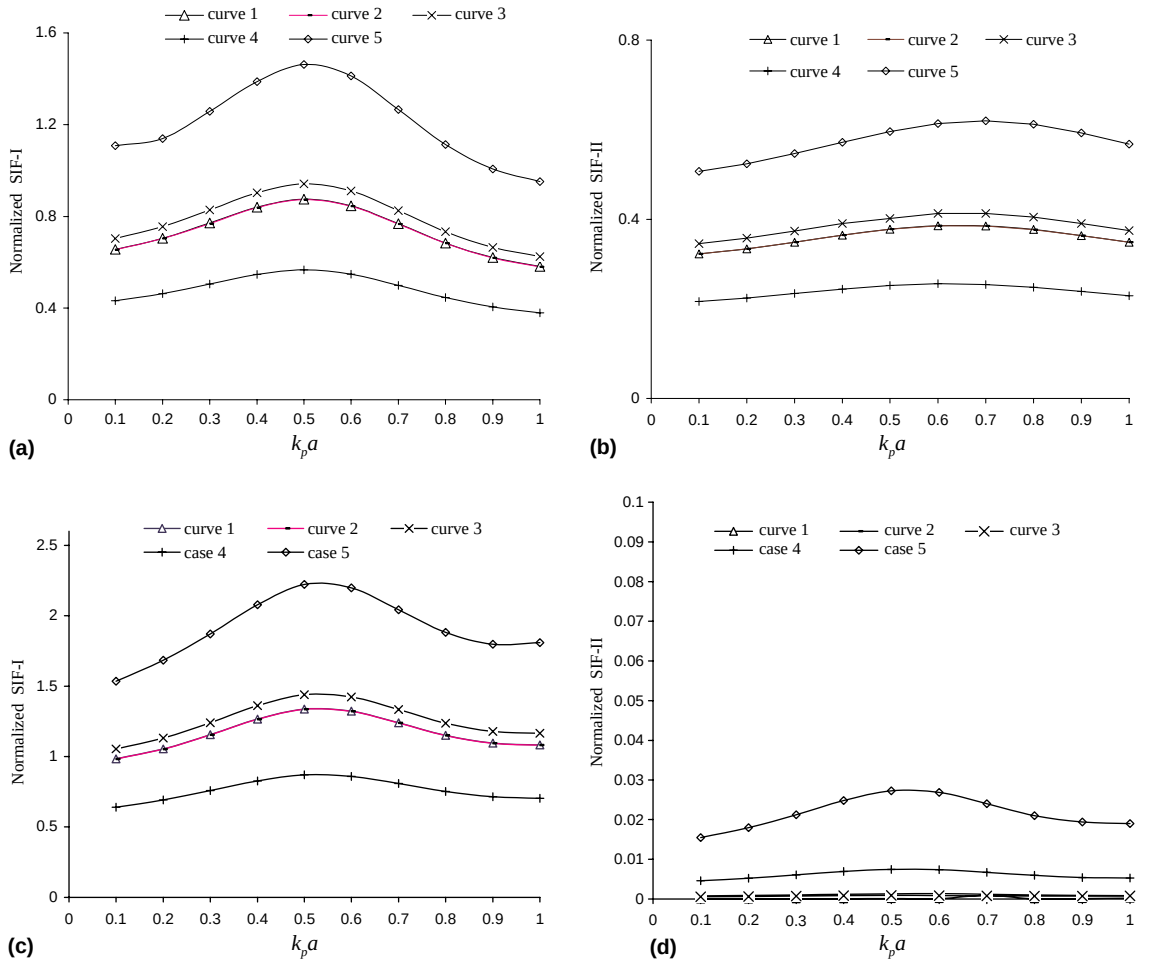

Fig. 3. SIF versus frequency at the left crack-tip of a crack inclined by $\varphi = 45°$ with respect to the Ox_1-axis and at fixed incident wave angle $\theta = \pi/2$. Curves 1–5 are as follows: 1: homogeneous case; 2 and 4: stiffening shear modulus across depths of $L = 520$ m and $L = 40$ m; 3 and 5: softening shear modulus across depths of $L = 520$ m and $L = 40$ m. Cases (a), (b) are for incident P-waves and cases (c), (d) are for SV-waves.

in the rapidly softening profile, of about 35% in the rapidly stiffening one, and less than 10% for the remaining cases. In sum, Figs. 3–5 clearly demonstrate that the influence of material inhomogeneity on elastic wave–crack interaction problems must be accounted for in order to obtain more accurate information on the dynamic stress fields that develop near the crack-tips.

It is well known that a crack in an otherwise homogeneous continuum swept by a travelling disturbance not only acts as a stress concentrator, but also as a wave scatterer. Thus, it is of interest to investigate how the presence of inhomogeneity affects the scattered displacement field. To that purpose, we introduce two observation points, A and B, with coordinates $(0, d/2)$ and $(0, 2d)$, respectively, where $d = -100$ m was the depth of the crack from the reference horizontal axis (see Fig. 1). A travelling P wave that forms an incident angle of $\theta = \pi/2$ with respect to the horizontal (i.e., moving directly upwards) is used, while the crack orientation is $\varphi = 45°$. The variation of the displacement amplitude (both real and imaginary parts), as it

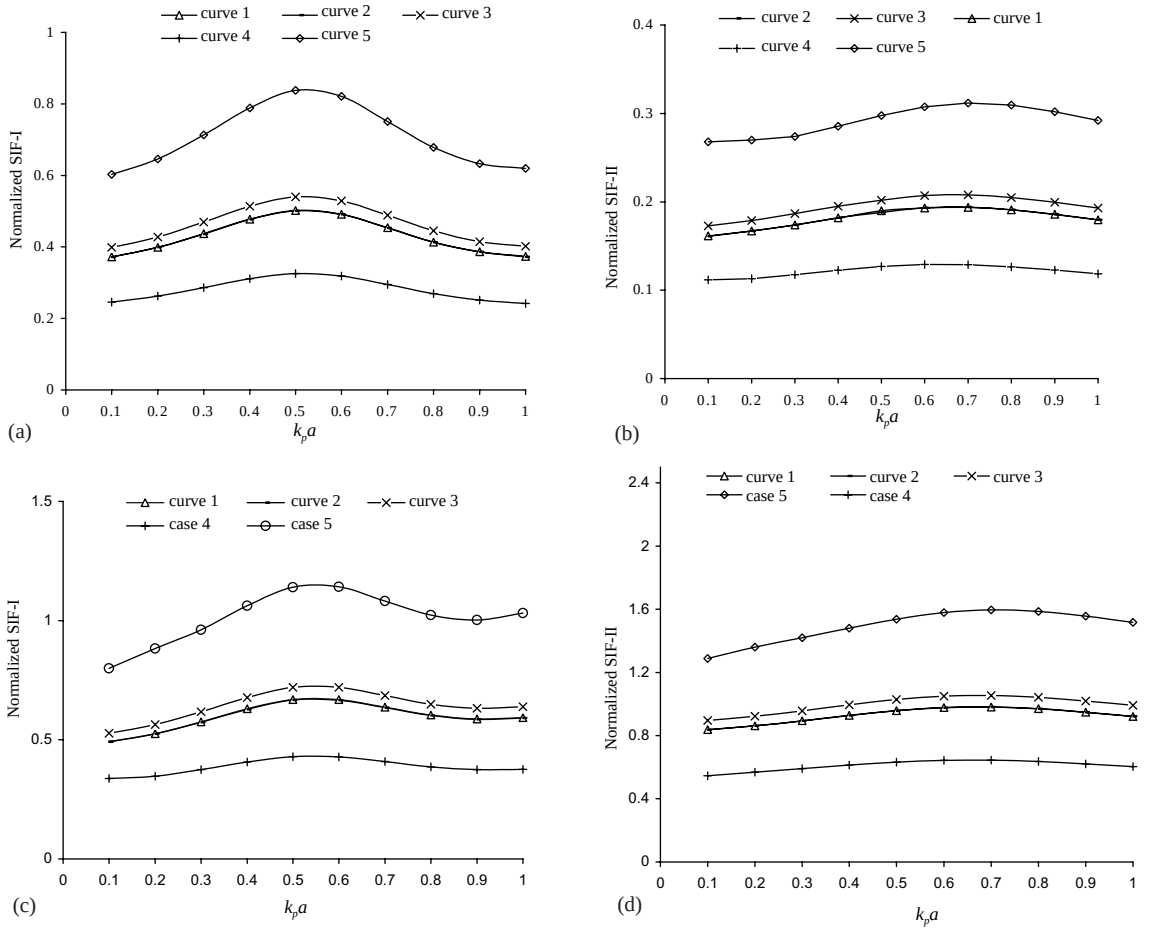

Fig. 4. SIF versus frequency at the left crack-tip of a crack inclined by $\varphi = 45°$ with respect to the Ox_1-axis and at fixed incident wave angle $\theta = \pi/3$. Curves 1–5 are as follows: 1: homogeneous case; 2 and 4: stiffening shear modulus across depths of $L = 520$ m and $L = 40$ m; 3 and 5: softening shear modulus across depths of $L = 520$ m and $L = 40$ m. Cases (a), (b) are for incident P-waves and cases (c), (d) are for SV-waves.

Table 1
Overshoot (as %) of SIF versus dimensionless frequency for the inhomogeneous medium

$k_P a$	P-wave			SV-wave		
	Case 1	Case 2	Case 4	Case 1	Case 2	Case 4
Mode I SIF						
0.1	68	7	−36	54	8	−35
0.5	68	8	−35	68	7	−33
1.0	60	8	−36	70	11	−32
Mode II SIF						
0.1	62	8	−31	1050	*	−250
0.5	58	6	−32	1250	*	−267
1.0	65	9	−33	1000	*	−250

Case 1: softening material, $L = 40$ m; Case 2: softening material, $L = 520$ m; Case 3: stiffening material, $L = 520$ m; Case 4: stiffening material, $L = 40$ m. (Note that the overshoot is negligible for Case 3; also, * indicates negligible values.)

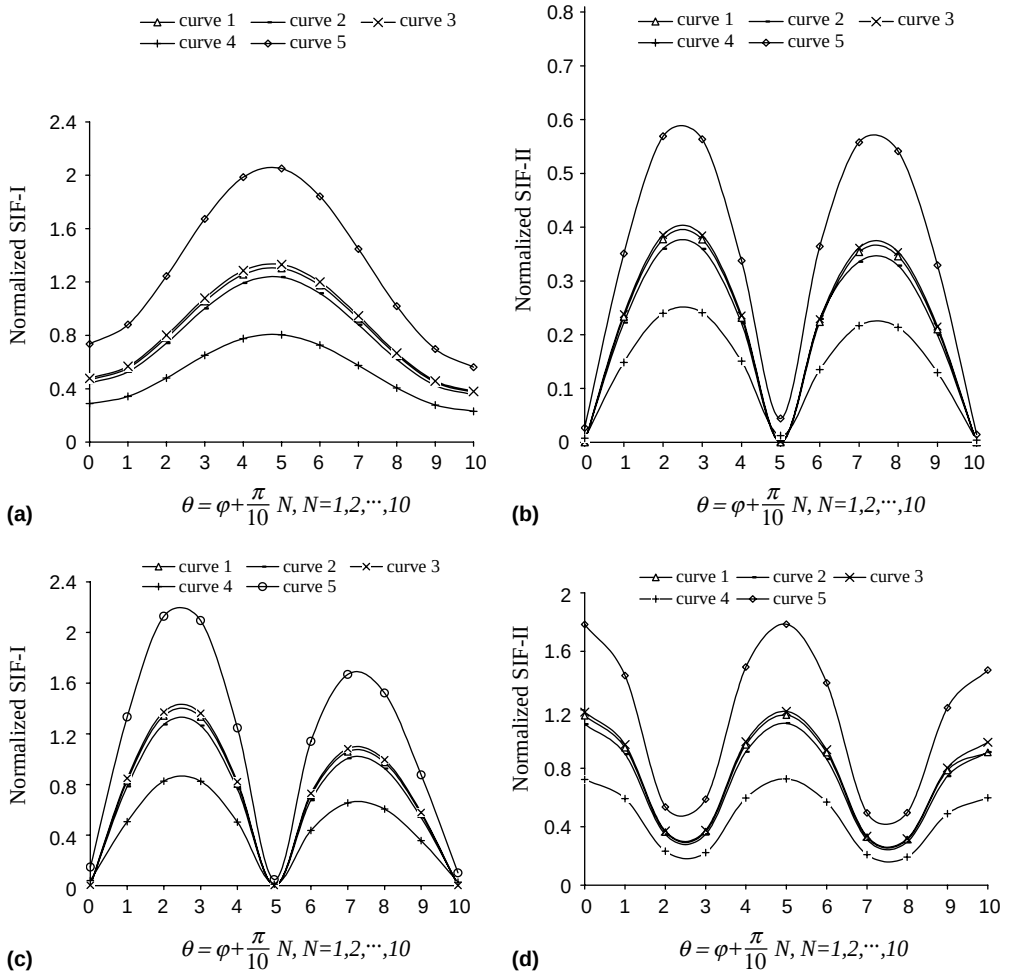

Fig. 5. SIF versus incident angle at the left crack-tip of a crack inclined by $\varphi = 45°$ with respect to the Ox_1-axis and at fixed frequency of $k_P\alpha = 5$. Curves 1–5 are as follows: 1: homogeneous case; 2 and 4: stiffening shear modulus across depths of $L = 520$ m and $L = 40$ m; 3 and 5: softening shear modulus across depths of $L = 520$ m and $L = 40$ m. Cases (a), (b) are for incident P-waves and cases (c), (d) are for SV-waves.

Table 2
Maximum overshoot (as %) in SIF at $k_P = 0.50$

	Mode I SIF		Mode II SIF	
	P-wave	SV-wave	P-wave	SV-wave
Case 1	42	56	49	55
Case 2	1	3	2	4
Case 3	−7	−5	−9	−3
Case 4	−38	−38	−37	−36

Case 1: softening material, $L = 40$ m; Case 2: softening material, $L = 520$ m; Case 3: stiffening material, $L = 520$ m; Case 4: stiffening material, $L = 40$ m.

propagates through the medium in the absence of a crack with dimensionless frequency $k_P\alpha$ (ranging from 0.1 to 2.0), is given in Figs. 6 and 8 for the two aforementioned observation stations. Three basic cases are considered, namely the inhomogeneous material with a softening shear modulus (curve 1), the background homogeneous material (curve 2) and the inhomogeneous material with a stiffening shear modulus (curve 3), where in both cases the modulus variation is defined across the short depth scale of $L = 40$ m. The scattered displacement field that develops because of wave-crack interaction is finally shown in Figs. 7 and 9 for observation points A and B, respectively, and for the same cases as before.

The following points may now be made: (a) The incident wave travels with increasing amplitude at higher frequencies, while the presence of inhomogeneity decreases/increases the vertical amplitude (u_2) as the shear modulus profile becomes stiffer/softer in the direction of propagation. As the wave reaches more distant stations, (i.e., goes from A to B), the effect of inhomogeneity is cumulative in the sense that displacements increase even more for the softening profile (and vice versa for the stiffening profile). Since the ratio of the real to imaginary displacements remains nearly constant, there is relatively little signal dispersion with distance, which is a consequence of this rather special type of inhomogeneous material with macroscopically constant wave speeds. (b) The presence of a line crack, inclined by 45° to the path of the

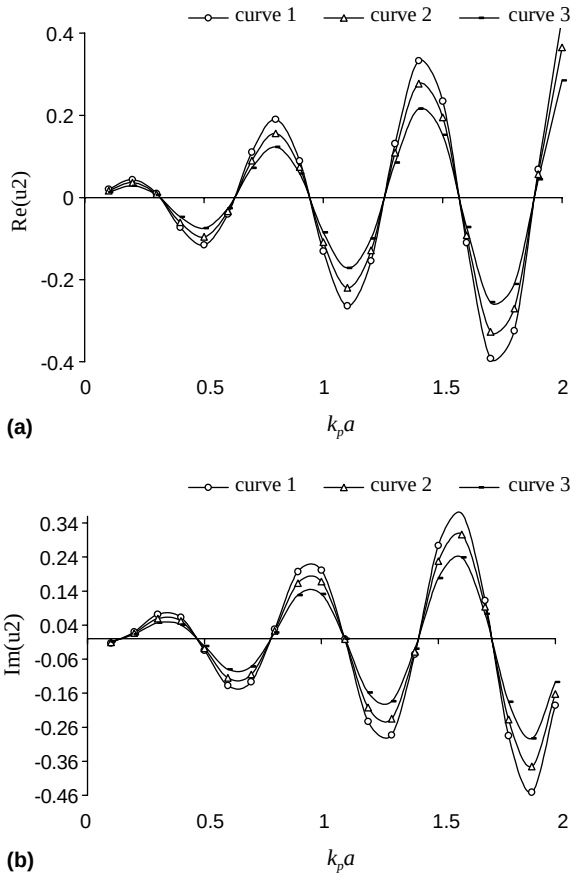

Fig. 6. Incident P-wave field at observation point $(0, -50)$ versus frequency for an incident angle $\theta = \pi/2$. Curves 1–3 respectively are for the softening, the homogeneous and the stiffening material, with cases: (a) Re(u_2) displacement; (b) Im(u_2) displacement.

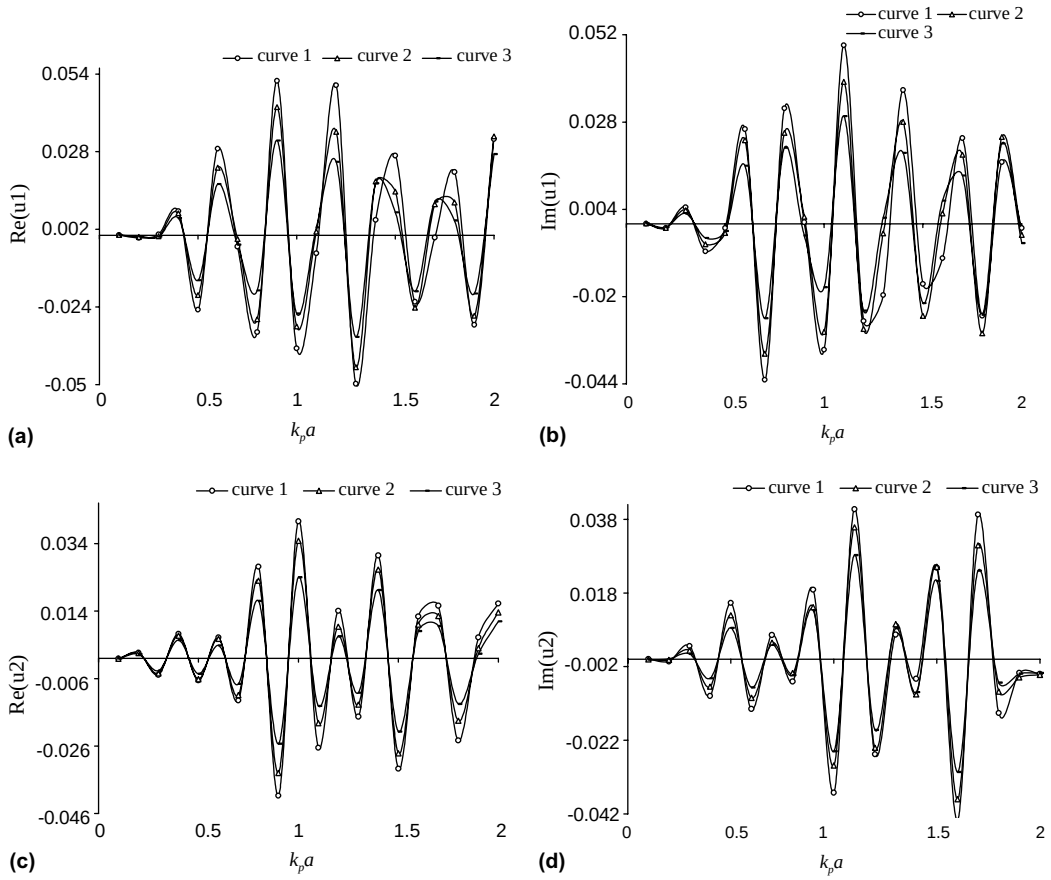

Fig. 7. Scattered wave field at observation point $(0, -50)$ versus frequency for an incident angle $\theta = \pi/2$ and a crack inclination angle $\varphi = \pi/4$. Curves 1–3 respectively are for the softening, the homogeneous and the stiffening material, with cases: (a) $\mathrm{Re}(u_1)$ displacement; (b) $\mathrm{Im}(u_1)$ displacement; (c) $\mathrm{Re}(u_2)$ displacement; (d) $\mathrm{Im}(u_2)$ displacement.

propagating wave, complicates the picture significantly. First we note the emergence of a sizeable horizontal component of motion (u_1) of the same magnitude as the vertical one. Next, we look at the observation point located above the crack (i.e., A), where we observe that the previous rather smooth frequency variation of the incident wave is now disturbed, with peaks in the response followed by low points. The only consistent pattern of behavior here is that the spread between inhomogeneous (irrespective of the exact type) and homogeneous material is far less pronounced (but still detectable) than before. This indicates the relative importance of scattering in the presence of a crack versus inhomogeneity. The situation with observation point B located below the crack is different. There, frequency dependence of the displacement amplitude is more smooth and reminiscent of that exhibited by the incident wave. However, a sizeable difference remains between vertical and horizontal components, with the former showing a very smooth variation compared to the latter. Also, the relative importance of inhomogeneity is again re-established in the sense that the spread between inhomogeneous and homogeneous materials is quite wide, especially for the softening case. Table 3 summarizes some of these results by giving the maximum overshoot of inhomogeneous over homogeneous displacement response (real part) for both observation points, with and without the crack. In the case of point A, the overshoot range is 15–20% for the softening material and

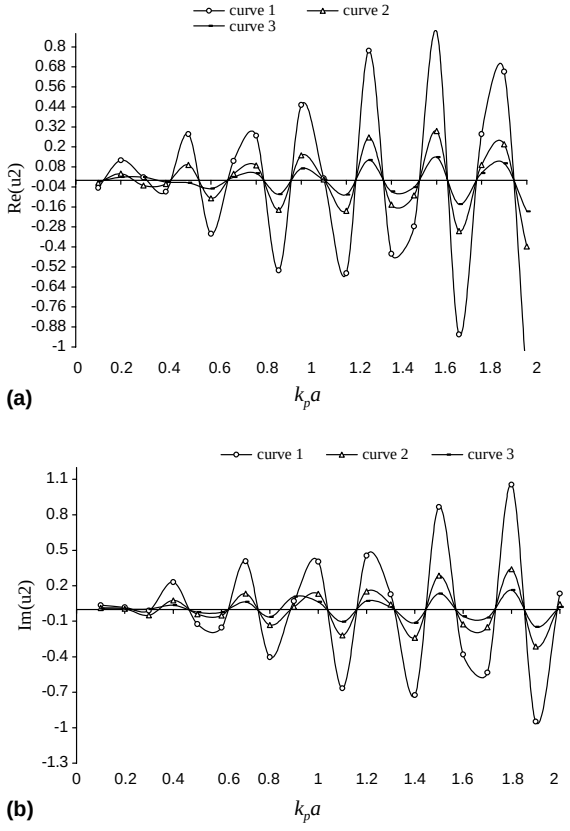

Fig. 8. Incident P-wave field at observation point $(0, -200)$ versus frequency for an incident angle $\theta = \pi/2$. Curves 1–3 respectively are for the softening, the homogeneous and the stiffening material, with cases: (a) $\mathrm{Re}(u_2)$ displacement; (b) $\mathrm{Im}(u_2)$ displacement.

-25% to -30% for the stiffening material. For point B, this overshoot increases substantially and the corresponding range is now 100-200% for the former material and -50% to -60% for the latter material.

5.5. Discussion

The parametric study presented in this section shows that graded materials may have a significant influence on both near-field stress concentrations and far-field scattered wave motions. The values of the dynamic SIFs that were computed were found to be quite sensitivity to (a) the frequency of the traveling incident wave and (b) the variation of the material constants with depth. Although a very particular type of imhomogeneous material was examined, whereby the elastic parameters and the density increase (or decrease) proportionally with depth and the material appears macroscopically constant exhibiting little dispersion, it seems plausible to argue that the same basic trends hold true for more general cases. This is a cause for concern regarding fracture and fatigue processes not only in geological materials, but also in any modern, functionally graded material with ramifications on their integrity and reliability during use. Furthermore, the recovery of scattered wave fields in fractured inhomogeneous continua is important in earthquake engineering for synthesis of artificial accelerograms and for soil–structure interaction studies. Finally, although the results obtained herein are for a restricted type of geological inhomogeneity, the methodology is applicable to different research fields such as non-destructive material testing and material science.

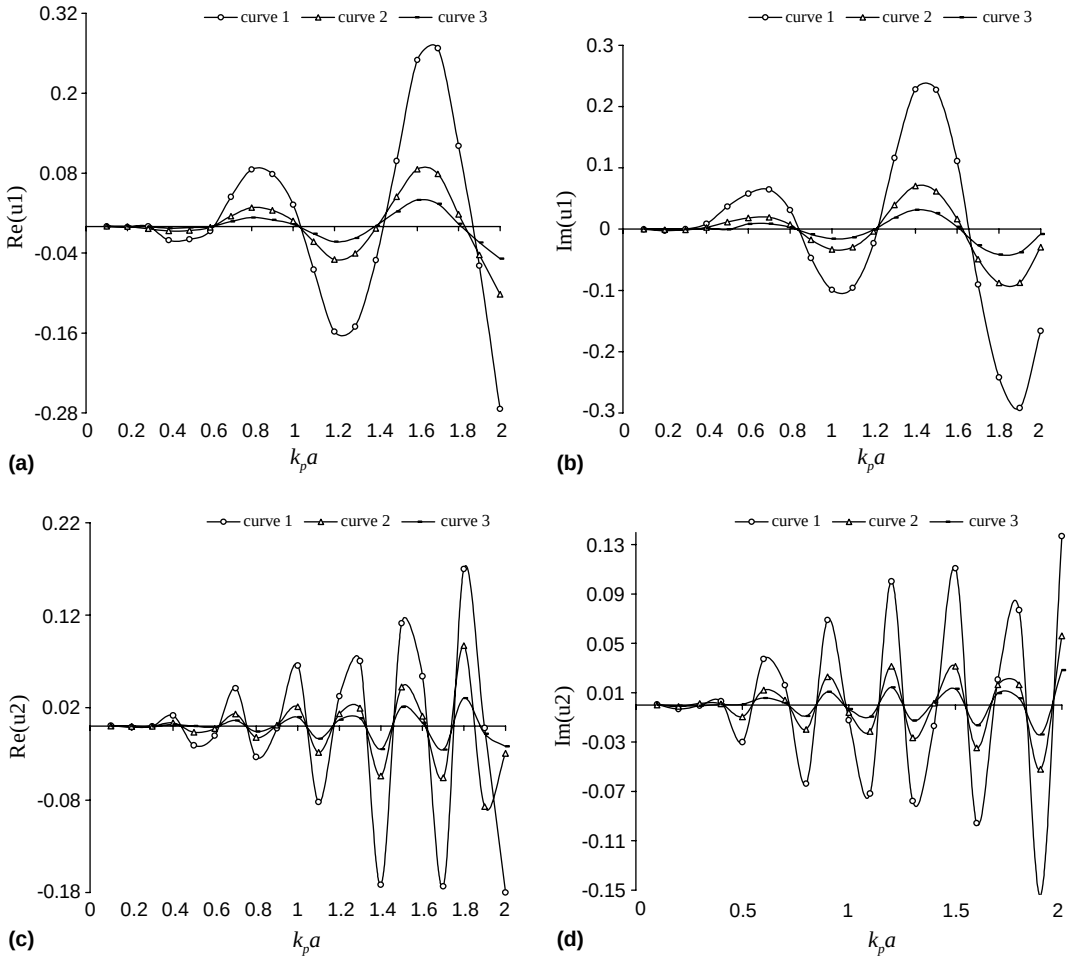

Fig. 9. Scattered wave field at observation point $(0, -200)$ versus frequency for an incident angle $\theta = \pi/2$ and a crack inclination angle $\varphi = \pi/4$. Curves 1–3 respectively are for the softening, the homogeneous and the stiffening material, with cases: (a) $\mathrm{Re}(u_1)$ displacement; (b) $\mathrm{Im}(u_1)$ displacement; (c) $\mathrm{Re}(u_2)$ displacement; (d) $\mathrm{Im}(u_2)$ displacement.

Table 3
Maximum overshoot (as %) in the real component of the displacement field u_i

	Observation point A			Observation point B		
	Incident u_2	Scattered u_1	Scattered u_2	Incident u_2	Scattered u_1	Scattered u_2
Case 1	13	20	16	200	208	94
Case 2	−24	−27	−30	−55	−50	−63

Case 1: softening material, $L = 40$ m; Case 4: stiffening material, $L = 40$ m.

6. Conclusions

The present work concerns the development of an efficient BIEM for numerical solution of 2D elastodynamic problems in cracked inhomogeneous media. The fundamental solutions entering the BIEM

formulation are derived through combination of an algebraic transformation procedure in conjunction with the Radon transform. They provide an exact representation of the displacement and traction fields in the particular inhomogeneous medium under study due to a point force oscillating under steady-state conditions. To the best of our knowledge, these solutions, at least in the form given herein, have not appeared in the literature to date. They are subsequently employed within the context of a non-hypersingular, traction BIEM for solution of wave propagation problems in non-homogeneous geological media with an internal crack. The accuracy and convergence characteristics of the present numerical method are gauged through the solution of a benchmark example. Subsequently, parametric studies are conducted regarding the dynamic response of an inclined crack, including sensitivity of both scattered displacement and stress wavefields that develop in the surrounding medium to the key problem parameters, namely degree of soil inhomogeneity, crack characteristics, type and orientation of the incident elastic waves. Finally, the present BIEM approach can be further developed and applied to more complex geological media, (with free-surface topography, layering and in the presence of interface cracks) or alternatively, to other categories of problems in mechanics, such as non-destructive testing evaluation of composite materials and of structural components.

Acknowledgements

The authors wish to acknowledge financial support provided through the NATO CST.ELG. 980303 grant.

References

Aliabadi, M., Rooke, D., 1991. Numerical Fracture Mechanics. Computational Mechanics Publication, Southampton.

Ang, W., Clements, D., Cooke, T., 1999. A hypersingular boundary integral equation for anti-plane crack problems for a class of inhomogeneous anisotropic elastic materials. Engineering Analysis with Boundary Elements 23, 567–572.

Ang, W.T., Clements, D., Vahdati, N., 2003. A dual-reciprocity BEM for a class of elliptic boundary-value problems for non-homogeneous anisotropic media. Engineering Analysis with Boundary Elements 27, 49–55.

Azis, M.I., Clements, D., 2001. A BEM for anisotropic inhomogeneous elasticity. International Journal of Solids and Structures 38, 5747–5763.

Babich, V.M., 1956. Ray Methods for the Computation of the Intensity of Wavefronts. Nauka Publications, Moscow.

Beskos, D.E., 1997. Boundary element methods in dynamic analysis, Part II (1986–1996). ASME Applied Mechanics Reviews 50, 149–197.

Bielak, J., MacCamy, R.C., McGhee, D.S., Barrry, A., 1991. Unified symmetric BEM–FEM for site effects on ground motions—SH waves. ASCE Journal of Engineering Mechanics 117, 2265–2285.

Chen, J., 1994. Time domain fundamental solution to Biot's complete equations of dynamic poroelasticity. I: 2D solution and II: 3D solution. International Journal of Solids and Structures 31, 1447–1490, 169–202.

Chen, E.P., Sih, G.C., 1977. Scattering waves about stationary and moving cracks. In: Sih, G.C. (Ed.), Mechanics of Fracture. In: Elastodynamic Crack Problems, vol. 4. Noordhoff Publishers, Leyden. Chapter 3.

Cruse, T.A., 1968. A direct formulation and numerical solution of the general transient elastodynamic problem: II. Journal of Mathematical Analysis and Application 22, 341–355.

Dineva, P.S., Gavrilova, E., 2000. Waves propagation in a multi-layered geological region. I: Non-elastic steady-state case and II: Transient case. International Journal on Seismology and Earthquake Engineering 2 (3), 11–21, 2(4), 1–8.

Dineva, P.S., Manolis, G.D., 2001. Scattering of seismic waves by cracks in multi-layered geological regions. I: Mechanical model and II: Numerical results. Soil Dynamics and Earthquake Engineering 21, 615–625, 627–641.

Dominguez, J., 1993. Boundary Elements in Dynamics. Elsevier Applied Science, London.

Ewing, W.M., Jardetzky, W.S., Press, F., 1957. Elastic Waves in Layered Media. Mc-GrawHill, New York.

Fah, D., Suhadolc, P., Panza, G.F., 1993. Variability of seismic ground motion in complex media: the case of a sedimentary basin in the Fruili (Italy) area. Journal of Applied Geophysics 30, 131–148.

Haskell, N.A., 1953. The dispersion of surface waves on multilayered media. Bulletin Seismological Society of America 43, 17–34.

Helbig, K. (Ed.), 1994. Modelling the Earth for Oil Exploration. Pergamon Press, London.
Herrera, I., 1964. On a method to obtain a Green's function for a multilayered half-space. Bulletin Seismological Society of America 54, 1087–1096.
Kausel, E., 1986. Wave propagation in anisotropic layered media. International Journal for Numerical Methods in Engineering 23, 1567–1578.
Kausel, E., 1981. An explicit solution for the Green's functions for dynamic loads in layered media. MIT Civil Engineering Research Report R81-13, MIT, Cambridge, Massachusetts.
Kim, S.M., Liao, S.T., Roesset, J.M., 1999. Simulation of the cross-hole method in isotropic and anisotropic media. International Journal for Numerical and Analytical Methods in Geomechanics 23, 1101–1119.
Knopoff, L., 1964. A matrix method of elastic wave problems. Bulletin Seismological Society of America 54, 431–438.
Ladyzenskaja, O., Urall'tzeva, N., 1973. Linear and Quasilinear Equations of Elliptic Type. Nauka Publication, Moscow.
Lahey Fortran 95, 2000. Lahey Computing Systems, Incline Village, Nevada.
Lie, S.T., Yu, G., Fan, S.C., 2000. Further improvement to the stability of the coupling BEM/FEM scheme for 2D elastodynamic problems. Computational Mechanics 25, 468–476.
Lysmer, J., Waas, G., 1972. Shear waves in plane infinite structures. ASCE Journal of Engineering Mechanics 98, 85–105.
Manolis, G.D., 2003. Elastic wave scattering around cavities in inhomogeneous continua by the BEM. Journal of Sound and Vibration 226 (2), 281–305.
Manolis, G.D., Beskos, D.E., 1987. Boundary Element Methods in Elastodynamics. Allen and Unwin, London.
Manolis, G.D., Shaw, R.P., 1996. Green's function for the vector wave equation in a mildly heterogeneous continuum. Wave Motion 24, 59–83.
Manolis, G.D., Shaw, R.P., 2000. Fundamental solutions for variable density two-dimensional elastodynamic problems. Engineering Analysis with Boundary Elements 24, 739–750.
Manolis, G.D., Rangelov, T.V., Shaw, R.P., 2003. The non-homogeneous biharmonic plate equation: fundamental solutions. International Journal of Solids and Structures 40, 5753–5767.
Mathematica, Version 3.0, 1996. Wolfram Research, Champaign, Illinois.
Mikhailov, S.E., 2002. Localized boundary-domain integral formulations for problems with variable coefficients. Engineering Analysis with Boundary Elements 26, 681–690.
Moczo, P., Bystricky, E., Kristek, E., Carcione, M., Bouchon, M., 1997. Hybrid modeling of P–SV seismic motion at inhomogeneous viscoelastic topographic structure. Bulletin of the Seismological Society of America 87, 1305–1323.
Nayfeh, A.H., 1995. Wave Propagation in Layered Anisotropic Media. North-Holland, Amsterdam.
Nowacki, W.K., 1978. Stress Waves in Nonelastic Solid. Pergamon Press, Oxford.
Panza, G.F., 1985. Synthetic seismograms: the Rayleigh waves modal summation. Journal of Geophysics 58, 125–145.
Panza, G.F., Romanelli, F., Vaccari, F., 2000. Seismic wave propagation in laterally heterogeneous anelastic media: theory and applications to seismic zonation. Advances in Geophysics 43, 1–95.
Pao, Y.H., Gajewski, R.R., 1977. The generalized ray theory and transient responses of layered elastic solids. Physical Acoustics 13, 183–265.
Rangelov, T.V., Dineva, P.S., Gross, D., 2003. A hypersingular traction boundary integral equation method for stress intensity factor computation in a finite cracked body. Engineering Analysis with Boundary Elements 27, 9–21.
Schwab, F., Knopoff, L., 1970. Surface wave dispersion computations. Bulletin Seismological Society of America 60, 321–344.
Song, C., Wolf, J.P., 1998. The scaled boundary finite element method: analytical solution in the frequency domain. Computer Methods in Applied Mechanics and Engineering 164, 249–264.
Sotiropoulos, D.A., 1993. Dispersion of elastic waves in periodically inhomogeneous media. Computational Mechanics 12, 134–146.
Tadeu, A., Kausel, E., Vrettos, C., 1996. Scattering of waves by subterranean structures via the BEM. Soil Dynamics and Earthquake Engineering 15, 387–397.
Tadeu, A., Godinho, L., Santos, P., 2002. Wave motion between two fluid-filled boreholes in an elastic medium. Engineering Analysis with Boundary Elements 26, 101–117.
Thomson, W.T., 1950. Transmission of elastic waves through a stratified solid. Journal of Applied Physics 21, 89–93.
Vainberg, B., 1982. Asymptotic Methods in Equations of Mathematical Physics. Moscow State University Publication, Moscow.
Vladimirov, V., 1984. Equations of Mathematical Physics. Mir Publishers, Moscow.
Vrettos, C., 1990. Dispersive SH-surface waves in soil deposits of variable shear modulus. Soil Dynamics and Earthquake Engineering 9, 255–264.
Vrettos, C., 1991. In-plane vibrations of soil deposits with variable shear modulus. II: Line load. International Journal for Numerical and Analytical Methods in Geomechanics 14, 649–662.
Wang, C.Y., Achenbach, J.D., 1993. A new method to obtain 3-D Green's functions for anisotropic solids. Wave Motion 18, 273–289.
Wang, C.Y., Achenbach, J., 1994. Elastodynamic fundamental solutions for anisotropic solids. Geophysics Journal International 118, 384–392.

Wendland, W., Stephan, E., 1990. A hypersingular boundary integral method for two-dimensional screen and crack problems. Archives of Rational Mechanics and Analysis 112, 363–390.

Yue, Z.Q., Xiao, H.T., Tham, L.G., 2003. Boundary element analysis of crack problems in functionally graded materials. International Journal of Solids and Structures 40, 3273–3291.

Zayed, A., 1996. Handbook of Generalized Function Transformations. CRC Press, Boca Raton, Florida.

Zhang, C., Gross, D., 1998. On Wave Propagation in Elastic Solids with Cracks. Computational Mechanics Publications, Southampton.

Zhang, C., Sladek, J., Sladek, V., 2003. Effects of material gradients on transient dynamic mode-III stress intensity factors in FGM. International Journal of Solids and Structures 40, 5251–5270.